Analytical and experimental determination of signal-to-noise ratio and figure of merit in three phase-contrast imaging techniques

P. C. Diemoz, A. Bravin, M. Langer, P. Coan

Analytical and experimental determination of signal-to-noise ratio and figure of merit in three phase-contrast imaging techniques

P.C. Diemoz,[1,2,3] A. Bravin,[2] M. Langer,[2,4] and P. Coan[1,5,*]

[1]*Faculty of Physics, Ludwig-Maximilians-Universität München, 85748 Garching, Germany*
[2]*European Synchrotron Radiation Facility, 38043 Grenoble, France*
[3] *Present address: Department of Medical Physics, University College London, WC1E 6BT London, UK*
[4]*CREATIS, Université de Lyon 1, CNRS UMR5220, INSERM U1044, INSA-Lyon, F-69621 Villeurbanne, France*
[5] *Faculty of Medicine, Ludwig-Maximilians-Universität München, 81377 Munich, Germany*
[*]*paola.coan@physik.uni-muenchen.de*

Abstract: We present a theoretical and experimental comparison of three X-ray phase-contrast techniques: propagation-based imaging, analyzer-based imaging and grating interferometry. The signal-to-noise ratio and the figure of merit are quantitatively compared for the three techniques on the same phantoms and using the same X-ray source and detector. Principal dependencies of the signal upon the numerous acquisition parameters, the spatial resolution and X-ray energy are discussed in detail. The sensitivity of each technique, in terms of the smallest detectable phase shift, is also evaluated.

OCIS codes: (110.7440) X-ray imaging; (110.2990) Image formation theory; (100.2960) Image analysis; (110.4980) Partial coherence in imaging.

References and links

1. A. Momose, T. Takeda, Y. Itai, and K. Hirano, "Phase-contrast X-ray computed tomography for observing biological soft tissues," Nat. Med. **2**(4), 473–475 (1996).
2. A. Snigirev, I. Snigireva, V. Kohn, S. Kuznetsov, and I. Schelokov, "On the possibility of x-ray phase contrast microimaging by coherent high-energy synchrotron radiation," Rev. Sci. Instrum. **66**(12), 5486–5492 (1995).
3. S. W. Wilkins, T. E. Gureyev, D. Gao, A. Pogany, and A. W. Stevenson, "Phase-contrast imaging using polychromatic hard X-rays," Nature **384**(6607), 335–338 (1996).
4. T. Davis, D. Gao, T. Gureyev, A. Stevenson, and S. Wilkins, "Phase-contrast imaging of weakly absorbing materials using hard X-rays," Nature **373**(6515), 595–598 (1995).
5. T. E. Gureyev and S. W. Wilkins, "Regimes of X-ray phase-contrast imaging with perfect crystals," Nuovo Cim. **19D**, 545–552 (1997).
6. D. Chapman, W. Thomlinson, R. E. Johnston, D. Washburn, E. Pisano, N. Gmür, Z. Zhong, R. Menk, F. Arfelli, and D. Sayers, "Diffraction enhanced x-ray imaging," Phys. Med. Biol. **42**(11), 2015–2025 (1997).
7. C. David, B. Nöhammer, H. Solak, and E. Ziegler, "Differential X-ray phase contrast imaging using a shearing interferometer," Appl. Phys. Lett. **81**(17), 3287–3289 (2002).
8. T. Weitkamp, A. Diaz, C. David, F. Pfeiffer, M. Stampanoni, P. Cloetens, and E. Ziegler, "X-ray phase imaging with a grating interferometer," Opt. Express **13**(16), 6296–6304 (2005).
9. F. Pfeiffer, T. Weitkamp, O. Bunk, and C. David, "Phase retrieval and differential phase-contrast imaging with low-brilliance X-ray sources," Nat. Phys. **2**(4), 258–261 (2006).
10. A. Olivo, K. Ignatyev, P. R. T. Munro, and R. D. Speller, "Noninterferometric phase-contrast images obtained with incoherent x-ray sources," Appl. Opt. **50**(12), 1765–1769 (2011).
11. P. C. Diemoz, A. Bravin, and P. Coan, "Theoretical comparison of three X-ray phase-contrast imaging techniques: propagation-based imaging, analyzer-based imaging and grating interferometry," Opt. Express **20**(3), 2789–2805 (2012).
12. M. R. Teague, "Irradiance moments - their propagation and use for unique retrieval of phase," J. Opt. Soc. Am. **72**(9), 1199–1209 (1982).
13. T. E. Gureyev, Y. I. Nesterets, A. W. Stevenson, P. R. Miller, A. Pogany, and S. W. Wilkins, "Some simple rules for contrast, signal-to-noise and resolution in in-line x-ray phase-contrast imaging," Opt. Express **16**(5), 3223–3241 (2008).

#172142 - $15.00 USD Received 10 Jul 2012; revised 2 Sep 2012; accepted 8 Sep 2012; published 29 Nov 2012

14. K. M. Pavlov, T. E. Gureyev, D. Paganin, Y. I. Nesterets, M. J. Morgan, and R. A. Lewis, "Linear systems with slowly varying transfer functions and their application to x-ray phase-contrast imaging," J. Phys. D Appl. Phys. **37**(19), 2746–2750 (2004).
15. P. C. Diemoz, P. Coan, I. Zanette, A. Bravin, S. Lang, C. Glaser, and T. Weitkamp, "A simplified approach for computed tomography with an X-ray grating interferometer," Opt. Express **19**(3), 1691–1698 (2011).
16. M. Bech, "X-ray imaging with a grating interferometer," PhD Thesis, University of Copenhagen (2009).
17. M. Sanchez del Rio, C. Ferrero, and V. Mocella, "Computer simulations of bent perfect crystal diffraction profiles," Proc. SPIE **3151**, 312–323 (1997), http://www.esrf.eu/UsersAndScience/Experiments/TBS/SciSoft/xop2.3.
18. W. Yashiro, Y. Takeda, and A. Momose, "Efficiency of capturing a phase image using cone-beam x-ray Talbot interferometry," J. Opt. Soc. Am. A **25**(8), 2025–2039 (2008).
19. V. Revol, C. Kottler, R. Kaufmann, U. Straumann, and C. Urban, "Noise analysis of grating-based x-ray differential phase contrast imaging," Rev. Sci. Instrum. **81**(7), 073709 (2010).
20. P. Modregger, B. R. Pinzer, T. Thüring, S. Rutishauser, C. David, and M. Stampanoni, "Sensitivity of X-ray grating interferometry," Opt. Express **19**(19), 18324–18338 (2011).
21. P. Coan, A. Peterzol, S. Fiedler, C. Ponchut, J. C. Labiche, and A. Bravin, "Evaluation of imaging performance of a taper optics CCD 'FReLoN' camera designed for medical imaging," J. Synchrotron Radiat. **13**(3), 260–270 (2006).
22. B. L. Henke, E. M. Gullikson, and J. C. Davis, "X-ray interactions: photoabsorption, scattering, transmission, and reflection at E=50-30000 eV, Z=1-92," At. Data Nucl. Data Tables **54**(2), 181–342 (1993).
23. T. Matsushita and H. Hashizume, "X-Ray monochromators," in *Handbook on Synchrotron Radiation*, E. Koch, ed. (North Holland Publishing Company, New York, 1983), pp. 261–314.
24. P. Coan, E. Pagot, S. Fiedler, P. Cloetens, J. Baruchel, and A. Bravin, "Phase-contrast X-ray imaging combining free space propagation and Bragg diffraction," J. Synchrotron Radiat. **12**(2), 241–245 (2005).
25. E. Pagot, S. Fiedler, P. Cloetens, A. Bravin, P. Coan, K. Fezzaa, J. Baruchel, J. Härtwig, K. von Smitten, M. Leidenius, M. L. Karjalainen-Lindsberg, and J. Keyriläinen, "Quantitative comparison between two phase contrast techniques: Diffraction Enhanced Imaging and Phase Propagation Imaging," Phys. Med. Biol. **50**(4), 709–724 (2005).
26. D. Shimao, H. Sugiyama, T. Kunisada, and M. Ando, "Articular cartilage depicted at optimized angular position of Laue angular analyzer by X-ray dark-field imaging," Appl. Radiat. Isot. **64**(8), 868–874 (2006).
27. M. J. Kitchen, D. M. Paganin, K. Uesugi, B. J. Allison, R. A. Lewis, S. B. Hooper, and K. M. Pavlov, "Phase contrast image segmentation using a Laue analyser crystal," Phys. Med. Biol. **56**(3), 515–534 (2011).
28. Y. I. Nesterets, P. Coan, T. E. Gureyev, A. Bravin, P. Cloetens, and S. W. Wilkins, "On qualitative and quantitative analysis in analyser-based imaging," Acta Crystallogr. A **62**(4), 296–308 (2006).
29. E. Pagot, "Quantitative comparison between two phase contrast techniques for mammography," PhD Thesis, Université Joseph Fourier, Grenoble (2004).

1. Introduction

X-ray phase-contrast imaging is a rapidly evolving research field. As opposed to conventional radiology, which derives image contrast from the differences in the X-ray attenuation properties of the imaged materials, phase-contrast techniques also rely on the wave phase shifts undergone by X-rays passing through an object. This possibility is particularly attractive for the imaging of samples made of light elements (e.g. soft biological tissues) and/or when high X-ray energies are used, which can result in very small attenuation contrast but non-negligible X-ray phase shift. Phase-contrast imaging methods are therefore very promising, in particular for applications in biology, medicine and materials science.

A number of phase-contrast techniques have been proposed and applied over the last twenty years [1–10], differing both in the setup and in the physical principles exploited for detecting the phase signal. In a recent publication [11], we have presented a comparison between different key parameters of the image formation in three phase-contrast techniques among the most applied and promising for biomedical applications: propagation-based imaging (PBI), analyzer-based imaging (ABI) and grating interferometry (GI). In particular, analytical expressions relating the signal-to-noise ratio (SNR) and the figure of merit (FoM) to the experimental and acquisition conditions were theoretically derived and compared.

A quantitative experimental comparison between these phase-contrast imaging methods in terms of detail visibility and clinically relevant parameters does not exist yet. Additionally, from published works using a single technique, it is not possible to extrapolate data for an a-posteriori comparison because of the large variety of experimental conditions applied to the different techniques. In principle, these parameters should be optimized in order to maximize

#172142 - $15.00 USD Received 10 Jul 2012; revised 2 Sep 2012; accepted 8 Sep 2012; published 29 Nov 2012

the sensitivity of the technique depending on the characteristics of both the sample to be investigated and the source/X-ray beam (e.g. source size and divergence, spatial and temporal coherence, energy etc). The objective of this work was to compare the three methods by using the same X-ray source and beam characteristics, the same imaging detector and test objects, and to study how the sensitivity would change if these parameters were to be modified. This work can help in choosing, among the three considered phase-contrast techniques, the most suitable one for given sample characteristics and experimental setup.

In the present article, we first recall the expressions for SNR and FoM and their validity conditions, and use them to derive analytical expressions for the phase sensitivity. Then we provide numerical estimates of the SNR and FoM for our PBI, ABI and GI experimental setups, and study the dependency of these quantities upon relevant acquisition parameters such as the system spatial resolution and the X-ray energy. An experimental comparison of the achievable FoM for the three considered phase-contrast imaging techniques is finally presented, which confirms the theoretical predictions.

2. Theory

We will briefly review the main features of the three techniques, and recall the expressions for the intensity registered by the detector as a function of the object attenuation, object phase shift and used acquisition parameters. Only the case of parallel beam geometry and of monochromatic radiation, characterized by a definite value of the wavelength λ, is considered here. The theoretical treatment for the ABI and GI techniques refers to their typical one-dimensional (1-D) implementation. However, the extension of the obtained formulas to 2-D geometries is straightforward. For sake of simplicity, we assume the case of a photon counting detector and a 100% detection efficiency.

In the following, we will indicate with z the optical axis, while the (x,y) coordinates define the object and detector planes.

Propagation-based imaging (PBI) [2, 3]. The sample is irradiated with highly spatially coherent X-rays, and the detector is set at a certain distance d from the sample. The perturbed wave interferes upon free-space propagation after the sample, according to Fresnel diffraction. This gives rise to typical interference fringes, localized at the edges of the different sample structures where variations in the phase shift arise. The intensity on the detector can be expressed by the transport of intensity equation (TIE) [12] in the near-field diffraction regime. The latter is valid when the absorption and phase shift are sufficiently slowly varying in the object plane (x,y) and/or when the propagation distance d is small [13]. In the case of quasi-homogeneous absorption in the object plane, the TIE can be further simplified and becomes:

$$I_{PBI} = I_0 T\left(1-\frac{\lambda d}{2\pi}\nabla_{\perp}^2\phi\right) \tag{1}$$

where the dependence upon the spatial variables (x,y) has been omitted for simplicity, and where I_{PBI} is the X-ray intensity incident on the detector, I_0 is the intensity incident on the sample, T is the sample transmission, and $\nabla_{\perp}^2\phi$ indicates the Laplacian in the (x,y) plane of the phase shift introduced by the sample.

The PBI technique requires the use of highly spatially-coherent radiation. However, as shown by Wilkins and associates [3], it is largely insensitive to even broad polychromaticity in the near-field diffraction regime, so that laboratory microfocus sources can be efficiently used.

Analyzer-based imaging (ABI) [4–6]. The sample is irradiated with parallel and quasi-monochromatic X-rays and a perfect crystal, placed downstream the sample and set at an angular position very close to the Bragg angle for diffraction, is used to analyze the radiation transmitted, scattered and refracted through the sample. Only X-rays incident in a very narrow angular range, defined by the so-called rocking curve (RC) of the analyzer crystal (which

#172142 - $15.00 USD Received 10 Jul 2012; revised 2 Sep 2012; accepted 8 Sep 2012; published 29 Nov 2012

features a full-width at half maximum on the order of several microradians), are diffracted onto the detector [6]. We will only consider here the case of a symmetrically-cut crystal, and we will assume that its diffraction plane corresponds to the plane (y,z). Under the geometrical optics approximation, which is valid for large values of the Takagi number [5, 14], the intensity incident on the detector can be expressed as:

$$I_{ABI} = I_0 T\, R\left(\theta_{an} + \Delta\theta_y\right) \tag{2}$$

where R is the analyzer RC [11], θ_{an} is the angular position of the analyzer crystal and $\Delta\theta_y = -\lambda/2\pi\left(\partial\phi/\partial y\right)$ is the component of the refraction angle in the direction y parallel to the crystal diffraction plane.

The ABI technique requires a parallel and quasi-monochromatic beam incident onto the sample. Although the perfect crystal usually placed before the sample provides the necessary collimation/monochromatization of the beam, this goes at the expense of the available flux, which is significantly reduced. For this reason, until now the technique has been mainly used with synchrotron radiation.

Grating interferometry (GI) [7–9]. The sample is irradiated with highly spatially coherent X-rays, and the radiation transmitted through the object is analyzed by a pair of gratings. The first is generally a phase grating, made of lines of period p_1 which introduces a periodic phase shift onto the beam. Downstream of it, at one of the fractional Talbot distances d_{Talbot} for the considered wavelength λ, the pattern created by the phase grating gives rise to periodic fringes. These are analyzed by a second grating made of absorbing lines that have the same periodicity p_2 of the fringe pattern. Assuming that the grating lines are oriented in the x direction, and denoting with y_G the relative position of the two gratings in the perpendicular direction y, the intensity on the detector can be expressed as [15]:

$$I_{GI} = I_0 T_{GR} T\left[1 + V\sin\left(\psi + \frac{2\pi}{p_2} y_G + \frac{2\pi}{S}\Delta\theta_y\right)\right] = I_0 T_{GR} T G\left(y_G; \Delta\theta_y\right) \tag{3}$$

where T_{GR} is the average transmission factor of the gratings, V is the fringe visibility, ψ is the shift of the sinusoidal fringe profile measured when no object is present in the beam and $S = p_2/d_{Talbot}$ is the angle corresponding to one grating period.

The fringe visibility is strongly dependent on the projected source size $\sigma_{proj} = \sigma_{src} d_{Talbot}/L$, where σ_{src} is the standard deviation of the source intensity distribution (assumed Gaussian shaped) and L is the distance of the first grating from the source. If we assume that the gratings are defect-free and the transmission through their absorbing lines is equal to zero, V can be expressed as [16]:

$$V = \frac{8}{\pi^2} e^{-2\pi^2\left(\sigma_{proj}/p_2\right)^2} \sum_{n=1}^{\infty} \frac{1}{\left(2n-1\right)^2} e^{-2\pi^2\left(\sigma_{proj}/p_2\right)^2\left(4n^2-4n\right)} \simeq \frac{8}{\pi^2} e^{-2\pi^2\left(\sigma_{proj}/p_2\right)^2} \tag{4}$$

where the approximation on the right-hand side of Eq. (4) is valid if $\sigma_{proj}/p_2 > 1/2\pi$ (all the higher-order terms can be discarded in this case). High spatial coherence is therefore required, while moderate beam polychromaticity is less critical to image quality degradation in GI.

However, as demonstrated by Pfeiffer and associates [9], even conventional X-ray sources can be used for GI provided that an appropriate "source grating" is introduced. This grating has the effect of creating a multitude of self-coherent beams whose fringes sum constructively.

Thermal and mechanical stabilities are an important issue for both the ABI and GI setups because they make use of additional optical elements (perfect crystals and gratings, respectively) to analyze the radiation transmitted through the sample. This can be particularly

#172142 - $15.00 USD Received 10 Jul 2012; revised 2 Sep 2012; accepted 8 Sep 2012; published 29 Nov 2012

relevant especially when long acquisitions are carried out, like in computed tomography or multiple-image processing for phase retrieval.

2.1 Signal-to-noise ratio and figure of merit for an edge signal: definitions

While the absorption signal depends on the point-wise sample absorption properties and is characteristic of the sample bulk regions, the phase-contrast signal, due its differential nature, is formed at the boundaries between structures of the sample showing different refractive indices. In order to quantify the amplitude of this type of signal, it is useful to introduce the edge signal-to-noise ratio (SNR). Among the possible definitions, we chose the following two complementary SNRs [11]. The first quantity, that we will call peak edge SNR, can be defined as:

$$SNR_{edge\,peak} \equiv \frac{\sqrt{A}\left(I_{\max} - I_{\min}\right)}{\sqrt{2std^2\left(I_{back}\right)}} \simeq \frac{\sqrt{A}\left(I_{\max} - I_{\min}\right)}{\sqrt{2I_{back}}} \tag{5}$$

where I_{min} and I_{max} are the minimum and maximum intensities of a mean intensity profile across the edge, obtained by averaging the signal over n pixel rows in the direction parallel to the edge; A is the area defined as $A = np \cdot p$, where p is the pixel size (assumed square). I_{back} is the average intensity in a background region of area A, and $std\left(I_{back}\right)$ indicates its standard deviation. The right side of Eq. (5) is derived under the assumption that the noise is Poisson distributed (pure statistical noise).

The SNR is strongly dependent on the number of photons used for the image acquisition. To compare images acquired with different X-ray fluxes, a more appropriate quantity is the figure of merit $FoM \equiv SNR/\sqrt{D}$, corresponding to the SNR normalized to the radiation dose D delivered to the sample during the acquisition. The latter is proportional to the X-ray intensity incident on the sample, so that it can be written as $D = K_{dose} I_0$, where K_{dose} is a constant depending on the X-ray energy and on the sample geometry and composition. In the general case, K_{dose} cannot be calculated analytically but needs to be estimated with the use of Monte Carlo simulations. The FoM is independent of the X-ray flux, under the hypothesis that the noise is Poisson distributed, and can be expressed as:

$$FoM_{edge\,peak} = \frac{\sqrt{A}\left(I_{\max} - I_{\min}\right)}{\sqrt{2K_{dose} I_0 I_{back}}} \tag{6}$$

A second definition for the SNR can be introduced if, instead of the minimum and maximum values of the intensity, the integral of all the intensity values on a profile across the edge is considered. Let us assume that the edge is parallel to the axis x, i.e. that it is perpendicular to the sensitivity direction y of both the ABI and GI techniques. In analogy to Eq. (5), the integral edge SNR can then be defined as:

$$SNR_{int.edge} \equiv \frac{\int_{-a}^{+a} dy \int_{x_0}^{x_1} dx \left| I\left(x,y\right) - I_{back} \right|}{\sqrt{2\int_{-a}^{+a} dy \int_{x_0}^{x_1} dx\, I_{back}}} \tag{7}$$

where $2a$ is the length of the considered profile and $L_x = x_1 - x_0$ is its width in the direction parallel to the edge. The integral edge SNR has the advantage of taking into account also the extent of the edge, which is an important parameter for quantifying its visibility. The corresponding FoM is then given by:

#172142 - $15.00 USD Received 10 Jul 2012; revised 2 Sep 2012; accepted 8 Sep 2012; published 29 Nov 2012

$$FoM_{\text{int}.edge} = \frac{\int_{-a}^{+a} dy \int_{x_0}^{x_1} dx \left| I(x,y) - I_{back} \right|}{\sqrt{2K_{dose} I_0 \int_{-a}^{+a} dy \int_{x_0}^{x_1} dx I_{back}}} \tag{8}$$

2.2 Theoretical expressions for signal-to-noise ratio and figure of merit

In our previous work, we derived theoretical expressions for both the peak and integral edge FoMs for the three considered techniques, by combining Eqs. (1-3) with Eqs. (6) and (8) [11]. In the case of ABI and GI, the additional assumption of small refraction angles is considered, so that the functions *R* and *G* can be safely replaced by their linear approximation around $\Delta\theta_y = 0$ [6, 15].

The following expressions for the peak edge FoM can then be obtained [11]:

$$FoM_{PBI,peak} \simeq -\frac{\lambda d\sqrt{A}}{2\pi\sqrt{2K_{dose}}} \left(\nabla^2_{\max}\phi - \nabla^2_{\min}\phi \right) \tag{9}$$

$$FoM_{ABI,peak} \simeq \frac{\sqrt{A}}{\sqrt{2K_{dose}}} \frac{R'(\theta_{an})}{\sqrt{R(\theta_{an})}} \Delta\theta_y \tag{10}$$

$$FoM_{GI,peak} \simeq \frac{\sqrt{AT_{GR}}\, G'\left(y_G; \Delta\theta_y = 0\right)}{\sqrt{2K_{dose} G\left(y_G; \Delta\theta_y = 0\right)}} \Delta\theta_y = \sqrt{2}\pi \frac{\sqrt{AT_{GR}}}{\sqrt{K_{dose}}} \frac{Vd_{Talbot}}{p_2} \frac{\cos\left(\psi + \frac{2\pi}{p_2} y_G\right)}{\sqrt{1 + V\sin\left(\psi + \frac{2\pi}{p_2} y_G\right)}} \Delta\theta_y \tag{11}$$

The peak edge FoM for PBI is proportional to the difference of the phase Laplacian at the two sides of the edge, while the ABI and GI FoMs are proportional to the refraction angle. In the practical case of an extended source and a detector with finite spatial resolution, it must be noted that the measured refraction angle and phase are the convolution of their actual values with the point-spread function (PSF) of the imaging system, i.e., in Eqs. (9-11), $\Delta\theta_y = \Delta\theta_{y,ideal} * PSF$, $\nabla^2_{\max}\phi = \max\left(\nabla^2\phi_{ideal} * PSF\right)$ and $\nabla^2_{\min}\phi = \min\left(\nabla^2\phi_{ideal} * PSF\right)$.

ABI shows a strong dependence upon the angular position of the analyzer. In fact, the quantity $R'(\theta_{an})/\sqrt{R(\theta_{an})}$ is maximized at the end of the slopes of the RC, while it is minimum at the peak of the rocking curve (which we will henceforth call the 'top' position). This is shown in Fig. 1, where the RC (Fig. 1(a)), its first derivative (Fig. 1(b)) and the quantity $R'(\theta_{an})/\sqrt{R(\theta_{an})}$ (Fig. 1(c)) are reported, together with the plot of the RC second derivative (Fig. 1(d)). In the plots, the X-ray energy is 26 keV and the Si(333) reflection has been considered for both the monochromator crystal (placed before the sample) and the analyzer crystal. These correspond to the acquisition parameters used in our experimental setup (see section 3). The reported profiles have been calculated with XOP [17]. Under the considered experimental conditions, the FoM is strongly peaked at positions θ_{an} ~2 μrad (Fig. 1(c)).

#172142 - $15.00 USD Received 10 Jul 2012; revised 2 Sep 2012; accepted 8 Sep 2012; published 29 Nov 2012

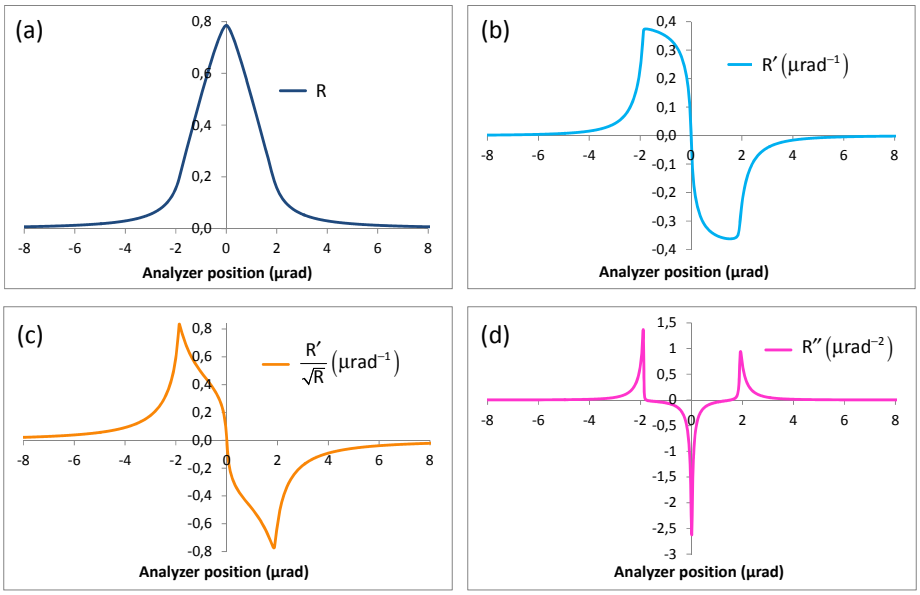

Fig. 1. (a) Theoretical ABI RC in the case of monochromator and analyzer in Si(333) Bragg reflection geometry, and for an X-ray energy of 26 keV. (b) First derivative of the RC, (c) ratio between the first derivative of the RC and its square root, (d) second derivative of the RC. The RC values have been calculated with XOP [17].

The expression derived for the FoM in GI is in agreement with the results presented in previous works [18–20]. The $SNR_{GI,peak} = \sqrt{I_0 K_{dose}}\, FoM_{GI,peak}$ in fact, increases with photon statistics, being proportional to the square root of the photon intensity (see Eq. (11)). Besides, the SNR and FoM also increase with the fringe visibility V and with the ratio d_{Talbot}/p, as obtained by Revol and associates [19] and Modregger and associates [20]. However, the image noise was shown to be independent of the used gratings positions when the phase stepping method is applied to separate the absorption, refraction and scattering contributions [19,20]. This is not the case if a single image is considered. Similarly to ABI, in fact, in GI the FoM is strongly dependent upon the gratings position y_G through the quantity $G'(y_G)/\sqrt{G(y_G)}$ (see Eq. (11)). In Fig. 2, the plots of G (Fig. 2(a)), G' (Fig. 2(b)), $G'(y_G)/\sqrt{G(y_G)}$ (Fig. 2(c)) and G'' (Fig. 2(d)) are reported, as a function of y_G/d_{Talbot}. A period of the second grating $p_2 = 2$ µm, a Talbot distance $d_{Talbot} = 125$ mm and a visibility $V = 0.34$ have been considered, which correspond to the parameters of our experimental setup (see section 3). For simplicity, the shift of the sinusoid ψ has been set to zero in the plots in Fig. 2.

#172142 - $15.00 USD Received 10 Jul 2012; revised 2 Sep 2012; accepted 8 Sep 2012; published 29 Nov 2012

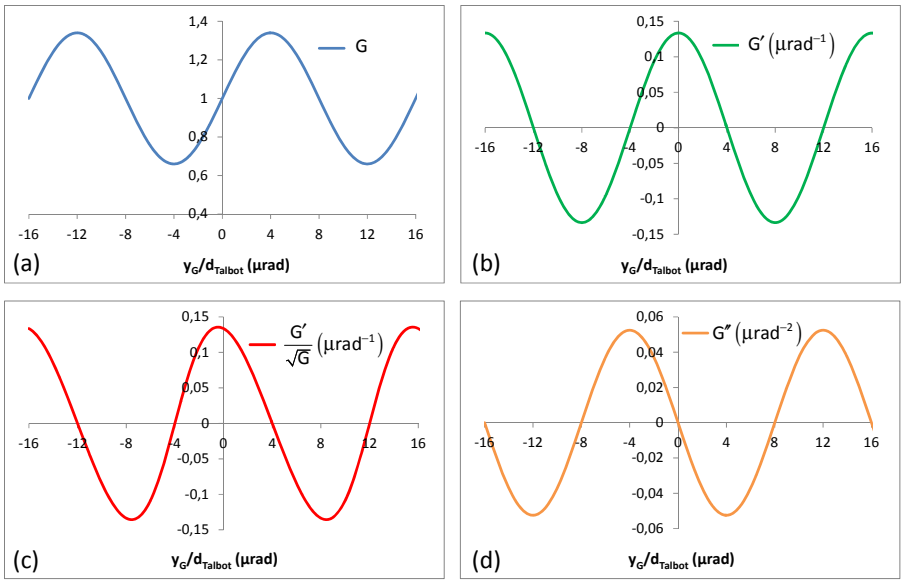

Fig. 2. (a) Plot of the function G in the GI technique, for a second grating period p_2 = 2 µm, a Talbot distance d_{Talbot} = 125 mm, a visibility V = 0.34 and a shift of the sinusoid ψ = 0. (b) First derivative of G, (c) ratio between the first derivative of G and its square root, (d) second derivative of G.

The quantity $G'(y_G)/\sqrt{G(y_G)}$ assumes its highest value at positions that are very close to the slopes of the function G, where the first derivative is maximized (see Fig. 2(c)). More precisely, we can observe from Eq. (11) that the FoM is highest when the function:

$$f = \frac{\sqrt{1+V\sin\left(\psi+\frac{2\pi}{p_2}y_G\right)}}{\left|\cos\left(\psi+\frac{2\pi}{p_2}y_G\right)\right|} \tag{12}$$

is minimized. It is easy to verify that this occurs when

$$\sin\left(\psi+\frac{2\pi}{p_2}y_G\right) = -\frac{1}{V}\left(1-\sqrt{1-V^2}\right) \tag{13}$$

and that, in this case, the function f is equal to:

$$f_{\min} = \frac{V}{\sqrt{2}}\frac{\sqrt[4]{1-V^2}}{\sqrt{V^2-1+\sqrt{1-V^2}}} \tag{14}$$

The maximum obtainable value for the peak edge FoM is therefore:

$$FoM_{GI,peak,\max} = 2\pi\frac{\sqrt{AT_{GR}}}{\sqrt{K_{dose}}}\frac{d_{Talbot}}{p_2}\frac{\sqrt{V^2-1+\sqrt{1-V^2}}}{\sqrt[4]{1-V^2}}\Delta\theta_y \tag{15}$$

The linear approximation of the functions R and G (here used to derive Eqs. (10) and (11), respectively in the ABI and GI techniques) is best satisfied at the slopes of these functions. At these positions, in fact, their first derivative is maximized (see Figs. 1(b) and 2(b)) and their

#172142 - $15.00 USD Received 10 Jul 2012; revised 2 Sep 2012; accepted 8 Sep 2012; published 29 Nov 2012

second derivative is equal to zero (see Figs. 1(d) and 2(d)). However, at the top position of the RC in ABI and at the top and bottom positions of the fringe period in GI, the first derivative is equal to zero and the second derivative is maximized. As it will also be shown on experimental images in section 4.2, the linear approximation is not appropriate in this case. A more accurate approximation is provided by a second-order Taylor expansion of the functions *R* and *G*. The following modified expressions for the peak edge FoM can thus be found for the top and bottom positions:

$$FoM_{ABI,peak,top} \simeq \frac{\sqrt{A}}{2\sqrt{2K_{dose}}} \frac{R''(\theta_{an})}{\sqrt{R(\theta_{an})}} \left(\Delta\theta_y\right)^2 \tag{16}$$

$$FoM_{GI,peak,top\ and\ bottom} \simeq \frac{\sqrt{AT_{GR}}}{2\sqrt{2K_{dose}}} \frac{G''\left(y_G;\Delta\theta_y=0\right)}{G\left(y_G;\Delta\theta_y=0\right)} \left(\Delta\theta_y\right)^2 \tag{17}$$

The FoM is in this case proportional to the squared value of the refraction angle and to the second derivative of the functions *R* and *G*.

In our previous work [11] analytical expressions for the integral edge FoM were also derived. We assume that the phase profile across the edge can be described as $\phi = -\left(H * P_{obj}\right)(y) \cdot \phi_{step}$, where ϕ_{step} is the total step in the phase shift across the edge, *H* is the Heavyside step function and $P_{obj} = \left(2\pi\sigma_{obj,y}^2\right)^{-1/2} \exp\left[-y^2/2\sigma_{obj,y}^2\right]$ is a normalized Gaussian function defining the smoothness of the object edge.

Analytical expressions for the integral edge FoM can be obtained by convolving the ideal intensity distribution (Eqs. (1-3) with the PSF of the imaging system, $P_{sys} = \left(2\pi\sigma_{sys,x}\sigma_{sys,y}\right)^{-1} \exp\left[-x^2/2\sigma_{sys,x}^2 - y^2/2\sigma_{sys,y}^2\right]$, and by developing Eq. (8):

$$FoM_{PBI,\mathrm{int}.edge} = 3.88 \cdot 10^{-2} \frac{d\lambda\sqrt{L_x}}{\sigma_{PBI}\sqrt{\sigma_{PBI}}\sqrt{K_{dose}}} \phi_{step} \tag{18}$$

$$FoM_{ABI,\mathrm{int}.edge} = 5.37 \cdot 10^{-2} \frac{\lambda\sqrt{L_x}}{\sqrt{\sigma_{ABI}K_{dose}}} \frac{R'(\theta_{an})}{\sqrt{R(\theta_{an})}} \phi_{step} \tag{19}$$

$$FoM_{GI,\mathrm{int}.edge} = 5.37 \cdot 10^{-2} \frac{\lambda\sqrt{L_x T_{GR}}}{\sqrt{\sigma_{GI}K_{dose}}} \frac{G'(y_G)}{\sqrt{G(y_G)}} \phi_{step} \tag{20}$$

where we have introduced the quantities: $\sigma_{PBI} \equiv \sqrt{\sigma_{sys.PBI,y}^2 + \sigma_{obj,y}^2}$, $\sigma_{ABI} \equiv \sqrt{\sigma_{sys.ABI,y}^2 + \sigma_{obj,y}^2}$ and $\sigma_{GI} \equiv \sqrt{\sigma_{sys.GI,y}^2 + \sigma_{obj,y}^2}$, with $\sigma_{sys.PBI,y}$, $\sigma_{sys.ABI,y}$ and $\sigma_{sys.GI,y}$ being the standard deviations in the *y* direction of the PBI, ABI and GI imaging system PSFs, respectively. The quantities σ_{PBI}, σ_{ABI} and σ_{GI} take into account the effect of both the imaging system PSF and the edge smoothness in increasing the width of the edge profiles. For all the techniques, the integral edge FoM is proportional to the edge phase step (see Eqs. (18-20).

2.3 Phase sensitivity

The integral edge FoM provides a way to directly compare the signal in the three phase-contrast techniques. It is in fact dependent on the same object parameter (i.e. the phase shift) in all three techniques. By making use of this important result (Eqs. (18-20), we will now proceed to a quantitative comparison of the PBI, ABI and GI sensitivities, by estimating in particular the smallest phase shift detectable by each of these techniques.

#172142 - $15.00 USD Received 10 Jul 2012; revised 2 Sep 2012; accepted 8 Sep 2012; published 29 Nov 2012

Let us consider an object detail providing a very weak phase signal and, for simplicity, negligible absorption. Therefore, the linear approximation for the RC and for the function *G* will be valid for ABI and GI, respectively. Let us also assume the case of near-field diffraction regime for PBI. Equations (18-20) can thus be used to describe the detail integral edge FoM.

Similarly to the case of conventional absorption imaging, the object detail is visible in the image if the modulus of the SNR associated to its boundaries is large enough to allow distinguishing the detail from the surrounding region (background). We can thus write, for instance in the case of PBI (see Eq. (18)):

$$\left|SNR_{PBI,\mathrm{int}.edge}\right| = \sqrt{I_0 K_{dose}}\left|FoM_{PBI,\mathrm{int}.edge}\right| = 3.88\cdot 10^{-2}\,\frac{d\lambda\sqrt{L_x I_0}}{\sigma_{PBI}\sqrt{\sigma_{PBI}}}\left|\phi_{step}\right| \geq K_{SNR} \quad (21)$$

where K_{SNR} is an arbitrary threshold. By inverting Eq. (21) we obtain:

$$\left|\phi_{step}\right| \geq \phi_{\min,PBI} \simeq 25.76\cdot\frac{K_{SNR}\sigma_{PBI}\sqrt{\sigma_{PBI}}}{d\lambda\sqrt{L_x I_0}} \quad (22)$$

The condition for the visibility of the detail is that the absolute value of the phase shift is larger than a certain minimum value; the latter, for a given setup, is inversely proportional to the square root of the beam intensity incident onto the object. This is not surprising since the image noise is directly related to the number of photon counts: if the exposure time is increased, smaller features in the object will therefore become visible.

In a similar way we obtain, for ABI and GI respectively:

$$\left|\phi_{step}\right| \geq \phi_{\min,ABI} = 18.62\cdot\frac{K_{SNR}\sqrt{R(\theta_{an})\sigma_{ABI}}}{\lambda\left|R'(\theta_{an})\right|\sqrt{L_x I_0}} \quad (23)$$

$$\left|\phi_{step}\right| \geq \phi_{\min,GI} = 18.62\cdot\frac{K_{SNR}\sqrt{G(y_G)\sigma_{GI}}}{\lambda\left|G'(y_G)\right|\sqrt{L_x T_{GR} I_0}} \quad (24)$$

If we now assume the intensity of the beam incident onto the object to be the same in the three cases, in order to deliver the same radiation dose to the sample, the ratio of the smallest detectable phase shift in PBI and ABI is given by:

$$\frac{\phi_{\min,PBI}}{\phi_{\min,ABI}} = 1.38\cdot\frac{\sigma_{PBI}\sqrt{\sigma_{PBI}}}{d\sqrt{\sigma_{ABI}}}\frac{\left|R'(\theta_{an})\right|}{\sqrt{R(\theta_{an})}} = \frac{FoM_{ABI,\mathrm{int}.edge}}{FoM_{PBI,\mathrm{int}.edge}} \quad (25)$$

The last part of Eq. (25) denotes the fact that the ratio between the two sensitivities is also equal to the ratio between the ABI and PBI integral edge FoMs obtainable for the same object detail (see Eqs. (18) and (19)).

The ratio of the smallest detectable phase shift in GI and ABI can be expressed by:

$$\frac{\phi_{\min,GI}}{\phi_{\min,ABI}} = \frac{\sqrt{\sigma_{GI}}}{\sqrt{T_{GR}\sigma_{ABI}}}\frac{\sqrt{G(y_G)}}{\left|G'(y_G)\right|}\frac{\left|R'(\theta_{an})\right|}{\sqrt{R(\theta_{an})}} = \frac{FoM_{ABI,\mathrm{int}.edge}}{FoM_{GI,\mathrm{int}.edge}} \quad (26)$$

for a generic working point respectively on the RC and on the function *G*. Note that $FoM_{ABI,int.edge}/FoM_{GI,int.edge}$ is also equal to the ratio between the two peak edge FoMs, $FoM_{ABI,peak}/FoM_{GI,peak}$, if $\sigma_{sys,ABI,y} \simeq \sigma_{sys,GI,y}$ (see Eqs. (10) and 11). If we consider only the positions where the sensitivity is maximized in ABI and GI, we can write:

#172142 - $15.00 USD Received 10 Jul 2012; revised 2 Sep 2012; accepted 8 Sep 2012; published 29 Nov 2012

$$\frac{\phi_{\min,GI}}{\phi_{\min,ABI}} = \frac{p_2}{2\sqrt{2}\pi\sqrt{T_{GR}}\,d_{Talbot}} \frac{\sqrt[4]{1-V^2}}{\sqrt{V^2-1+\sqrt{1-V^2}}} \frac{\left|R'\left(\theta_{an,\max}\right)\right|}{\sqrt{R\left(\theta_{an,\max}\right)}} \tag{27}$$

where $\theta_{an,max}$ indicates the analyzer position corresponding to the highest value of the FoM. In section 4.1, we will use Eqs. (25) and (27) to calculate the ratio of the smallest detectable phase shift in PBI, ABI and GI techniques for the parameters used in our experimental implementation. We will also describe how the sensitivities and their ratios for the different techniques (Eqs. (25-27) can be changed when the various acquisition parameters are modified.

3. Experimental setup and conditions

The experimental verification was carried out at the BM5 beamline of the European Synchrotron Radiation Facility (ESRF). The X-ray beam is produced by a bending magnet characterized by a magnetic field of 0.82 T; the source full-width at half maximum (FWHM) is about 270 μm (horizontal) × 80 μm (vertical) and the detector was placed at about 55 m from the source. X-rays with an energy of 26 keV (energy resolution $\Delta E/E \approx 10^{-4}$) were selected with a fixed-exit Bragg-Bragg double-crystal monochromator. The three different setups required by the PBI, ABI and GI techniques were mounted in turn, in order to image the same test objects in similar acquisition conditions. In all cases, images were recorded with the FReLoN CCD camera [21]. The effective pixel size at the sample position was about 7.5 μm.

The first test phantom consisted of two horizontal nylon wires with diameters of 200 μm and 350 μm, respectively. The values of the real and imaginary parts of the complex refractive index for nylon at 26 keV are: $\delta = 3.50 \cdot 10^{-7}$, $\beta = 1.29 \cdot 10^{-10}$ [22]. The beam attenuation at the centre of the two wires is therefore very low, respectively 0.7% and 1.2%, while the corresponding phase shifts are respectively 9.2 rad and 16.1 rad.

The second phantom was a Lucite parallelepiped of section 40 × 40 mm^2 and thickness 2.9 mm, in which a small groove is made (300 μm deep and 825 μm wide). The section of the hole can be well approximated by a circumference arc. Like the polymer wires, this groove produces very low absorption contrast (1.1%) with respect to the Lucite matrix, but a phase shift of 15.6 rad ($\delta = 3.94 \cdot 10^{-7}$ and $\beta = 1.39 \cdot 10^{-10}$ for Lucite at 26 keV [22]). The phantom was imaged with the groove oriented in the horizontal direction.

In the case of PBI, three sample-detector distances were considered: (7 ± 0.5) cm (almost pure absorption regime), (57 ± 1) cm, (150 ± 1) cm. When acquiring images with the ABI and GI techniques, the distance between the sample and the detector was set to (57 ± 1) cm. In order to avoid the contribution from "inline" phase-contrast, the propagation distance should be very small. However, this was not possible due to ABI and GI setups constraints. The propagation distance was chosen to be the same for ABI and GI for working under similar experimental conditions.

In ABI, two Si(333) crystals were used to further monochromatize the incoming beam and to analyze the beam exiting the object, respectively. The rotation axis (x) of the crystals was perpendicular to both the optical axis (z) and the vertical direction (y). The phantoms were imaged at the following positions of the analyzer RC (expressed as percentage of the maximum RC intensity): ± 10%, ± 50% and 100% (top) positions for the nylon wires, and ± 10%, ± 50% and + 90% positions for the groove.

For the GI acquisitions, a silicon π-shifting grating (G_1), with period p_1 = 3.99 μm and thickness t_1 = 34 μm, and a gold absorption grating (G_2) with period p_2 = 2.00 μm were used. The exact thickness of the gold lines in G_2 is unknown, but a conservative assumption is that it corresponds to an X-ray absorption of at least 90% at 26 keV. The two gratings were set with their lines oriented horizontally, so that the refraction sensitivity direction is vertical like in the case of ABI. The average intensity transmission through both gratings was calculated

#172142 - $15.00 USD Received 10 Jul 2012; revised 2 Sep 2012; accepted 8 Sep 2012; published 29 Nov 2012

theoretically to be about 50%. G_1 and G_2 were set at a mutual distance of 12.5 cm (3rd fractional Talbot distance for X-rays of 26 keV). It must be noted that this is not the optimal acquisition condition for GI, as larger distances would have provided a larger sensitivity (see section 4.1 below) at the used beamline. This choice, however, was determined by the geometry of the available pair of gratings. The periods p_1 and p_2 (designed in order to account for the beam divergence), together with the distance from the source (~55 m) dictate in fact a spacing between the gratings of about 125 mm. The measured fringes visibility (see Eq. (3)) was 34% in these experimental conditions. Phase-stepping acquisitions were performed by considering 9 equispaced grating positions along one fringe period.

The dose estimation was performed by using a calibrated ionization chamber (PTW semiflex 31002, PTW Freiburg, Germany) that was scanned through the incoming X-ray beam. The measured values for the skin dose in air are reported in Table 1 for all sets of acquisitions. The uncertainty in each measurement is ± 0.1 mGy. The variations of the dose for the three propagation distances in PBI and the two sides of the RC in ABI are due to variations over time of the X-ray beam flux.

Table 1. Measured values of the skin dose in air for the images acquisition

Measured skin dose in air (mGy)										
	PBI			ABI						GI
	7 cm	57 cm	150 cm	–10%	–50%	top	+ 90%	+ 50%	+ 10%	
Wires	93.6	49.7	73.1	62.5	32.8	26.4		37.2	80.2	183.0
Groove	89.6	56.3	72.5	76.6	35.6		25.6	39.5	76.6	79.6

4. Results and discussion

4.1 Estimation of the FoM

In the experimental conditions above described, the theoretical ratio between the ABI and PBI integral edge FoMs is 11.6 (see Eq. (25)), while that between ABI and GI ones is 8.7 (cf. Equation (27)). This means that, for the same dose delivered to the sample, ABI can detect phase variations 11.6 times smaller than those visible in PBI, and 8.7 times smaller than those visible in GI. In calculating these values, we have assumed the widths σ_{PBI}, σ_{ABI} and σ_{GI} (taking into account both the effect of the imaging system PSF and the smoothness of the object edge) to be essentially determined by the PSF of the detector, which is estimated to be around 15 μm (i.e. two pixels). As pointed out in section 2.3, the ratio between the ABI and GI integral edge FoMs is also equal to the ratio between the respective peak edge FoMs, if $\sigma_{ABI} \simeq \sigma_{GI}$ (see Eqs. (10-11) and (19-20). A general value for $FoM_{ABI,peak} / FoM_{PBI,peak}$, instead, cannot be calculated because the two terms depend on different quantities that are related to the imaged object ($FoM_{ABI,peak} \propto \Delta\theta_y$ and $FoM_{PBI,peak} \propto \nabla^2\phi$) (see Eqs. (9-10).

For the considered experimental parameters, the ratio between the ABI and GI sensitivities at the "top" (and also "bottom", for GI) positions of the RC and of the function *G*, respectively, can be calculated from Eqs. (16) and (17). ABI at these positions is in principle able to detect refraction angles that are 6.7 times smaller than those detectable in GI, for the same radiation dose to the sample.

It is important to remark that the sensitivities above estimated are dependent on the particular setup that was used and on the chosen acquisition parameters. The FoM for GI may be improved for higher-order Talbot distances, and the PBI FoM for higher sample-to-detector distances. The optimal working condition, however, is dependent on the source size, as we will discuss in the following. The ABI sensitivity can change as well if a different crystal reflection is chosen. A low-order reflection, for instance Si(111), would give a lower sensitivity, while higher-order ones, like Si(444), would provide larger sensitivities. In this case, in fact, the width of the RC will be smaller and its first derivative larger. As a

#172142 - $15.00 USD Received 10 Jul 2012; revised 2 Sep 2012; accepted 8 Sep 2012; published 29 Nov 2012

consequence, appropriate controller systems may be needed for improving the crystal stability.

Other relevant quantities affecting the sensitivity are the source projected size σ_{proj}, the width σ of the total object edge – imaging system PSF and the X-ray energy.

The effect of the smoothing operated by the parameter σ is more critical for PBI than it is for ABI and GI: $FoM_{PBI,int} \propto \sigma^{-3/2}$, while $FoM_{ABI\ and\ GI,int} \propto \sigma^{-1/2}$ (see Eqs. (18-20). However, the GI sensitivity is also affected by the source size through the dependency of the visibility upon σ_{proj} (see Eq. (4)). While a larger distance d_{Talbot} should improve the FoM as it decreases the angle corresponding to one grating period, $S = p_2 / d_{Talbot}$ (see Eq. (11)), this effect is counterbalanced by the increase of the projected source size (which decreases V). The optimal distance providing maximum sensitivity can be calculated numerically, and is equal to $d_{opt} \simeq 0.4\ p_2\ L / FWHM_{src} \simeq 0.17 p_2\ L / \sigma_{src}$ [20]. This implies for the BM5 beamline of the ESRF an optimal inter-grating distance of about 55 cm, if we assume perfect optical elements and grating lines oriented in the horizontal direction. At 26 keV, the 13th fractional Talbot distance (equal to 54 cm) can provide, in theory, a sensitivity 2.6 times better than that obtainable for the distance 12.5 cm used in the experiment.

It is useful to point out that, in the case a third "source grating" is used to shape the X-ray beam from an extended source, only the width of the produced small beams affects the visibility, while the total width of the source contributes to the blurring parameter σ.

The dependence of the sensitivity upon the X-ray energy is different for the three techniques. In PBI, according to Eq. (18), $SNR_{PBI,int} = \sqrt{I_0 K_{dose}}\, FoM_{PBI,int} \propto E^{-2}$ (the phase shift being inversely proportional to the energy, i.e. $\phi \propto E^{-1}$). In ABI, instead, $SNR_{ABI,int} = \sqrt{I_0 K_{dose}}\, FoM_{ABI,int} \propto E^{-1}$ because the analyzer angular sensitivity increases with the energy, approximately as $R'(\theta_{an}) / \sqrt{R(\theta_{an})} \propto E$ (Eq. (19)). In fact, the RC first derivative is approximately inversely proportional to the Darwin width of the crystal, which is in turn inversely proportional to the energy [23]. For GI, if the distance between the gratings is kept fixed (the optimal distance being independent of the energy) and if the visibility is assumed to be constant, again $SNR_{GI,int} = \sqrt{I_0 K_{dose}}\, FoM_{GI,int} \propto E^{-2}$ like in the PBI case. In a real experimental setup, however, the dependence of the visibility upon the energy cannot be neglected in general. The transmission through the absorbing lines in the second grating, indeed, can substantially differ from 0 in the case of high energies. This is a well-known problem: very high aspect-ratio gratings that are thick enough to absorb high energetic X-rays are technically challenging to be manufactured. A non-zero transmission through the absorbing lines can largely affect the fringe visibility and therefore the system sensitivity can be considerably decreased with respect to its theoretical values.

When very high X-ray energies are used, ABI may more easily provide high sensitivities compared to other phase-contrast imaging techniques. It therefore presents a big advantage for all those applications in which thick or high atomic number materials have to be investigated (e.g. some biomedical applications, such as imaging of whole and large human organs).

4.2 Experimental results

PBI, ABI and GI planar images of the two test phantoms (wires and groove) were acquired under the experimental and acquisition conditions described in section 3. All images have been normalized by using the corresponding "whitefield" and "darknoise" images (the first taken without the object in the beam, the latter with the detector not being illuminated). Expanded views of the 350 μm diameter wire and of the groove from PBI images recorded at the three considered sample-to-detector distances are reported in Fig. 3. For each object, the grayscale is the same for the three distances. It can be noted that the absorption and phase-

#172142 - $15.00 USD Received 10 Jul 2012; revised 2 Sep 2012; accepted 8 Sep 2012; published 29 Nov 2012

contrast signals for the groove and for the wire are reversed given the "reversed" shapes of the two objects.

When the propagation distance increases, the visualization of the object is improved because the magnitude of the X-ray interference fringes becomes larger. This is in agreement with what predicted by theory (Eq. (1)) in the case of propagation distances that are sufficiently small for the near-field diffraction regime to hold.

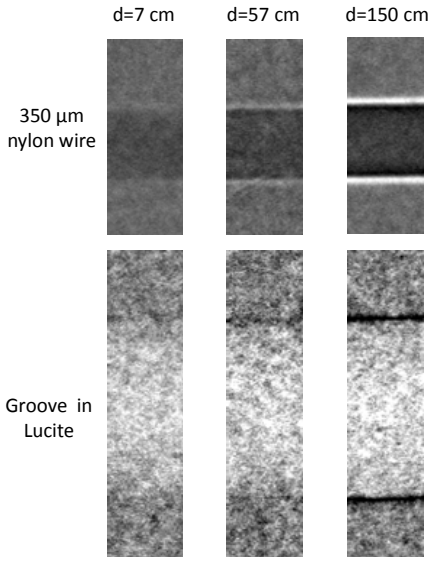

Fig. 3. PB images acquired at 3 different sample-to-detector distances: expanded views in small regions of interest in the 350 µm diameter nylon wire and in the groove in the Lucite phantom.

In order to quantitatively estimate the strength of the signal produced by the object edges relative to the background noise, we calculated the peak edge SNR following the definition in Eq. (5). The integral edge SNR definition is not appropriate in this case, because the full edge signal can be very wide due to the shape of the imaged objects and thus it can mix up with the absorption signal.

The maximum and minimum values for the intensity at the edges were calculated by averaging each of them over horizontal lines of 30 pixels. The average of several values of the background intensity, each one being the mean of the pixel counts over a different region of 30 pixels, and the related standard deviation, were also computed. The used SNRs (and their associated uncertainties) are the results of averaging calculations of the SNR (based on Eq. (5)) done in different regions of the image. Finally, the corresponding FoM was calculated by using the measured skin doses in air reported in Table 1. Results are shown in Fig. 4, for the top and bottom edges of the 200 µm diameter wire (Fig. 4(a)), of the 350 µm diameter wire (Fig. 4(b)) and of the small groove in Lucite (Fig. 4(c)). We can see that the increase of the FoM with the propagation distance is linear for all the considered objects, in agreement with Eq. (9), valid under the assumption of near-field diffraction regime. In the case of the groove, the FoM assumes negative values, since the edge signals are negative. The largest absolute values for the FoM are observed for the wires (slightly larger in the case of the thinner wire), while the smallest values are obtained for the groove.

#172142 - $15.00 USD Received 10 Jul 2012; revised 2 Sep 2012; accepted 8 Sep 2012; published 29 Nov 2012

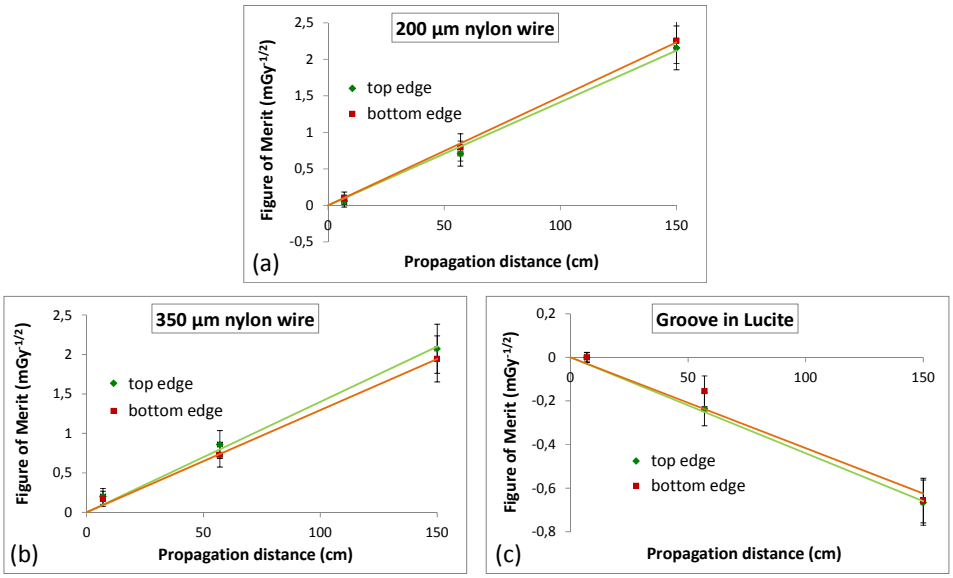

Fig. 4. Calculated values of the figure of merit (FoM) of the PBI edge signal for three different objects: (a) the 200 µm diameter nylon wire, (b) the 350 µm diameter nylon wire, (c) the groove in the Lucite phantom. Values at both the top and bottom edges are reported.

Images of the same test objects acquired with the ABI technique are presented in Fig. 5, for five different positions of the analyzer along its RC. The grayscale level has been adjusted independently for each of the images in order to optimize the object visualization. All images, (with the exception of the "top position" one) show opposite contrast at the two object edges. Unlike PBI, in ABI the signal is to a first approximation proportional to the refraction angle, which has opposite signs at the two edges. At the "top position", instead, as we have seen (Eq. (12)), the signal is proportional to the square of the refraction angle, which has the same value at the two object sides: the X-rays undergoing refraction at the two edges, in fact, are attenuated by the analyzer by the same amount.

Contrary to PBI, in ABI the objects absorption can hardly be evaluated from the raw unprocessed images, because the refraction signal is both very strong and more extended compared to that obtained in PBI. This is directly related to the signal dependence on the first derivative of the phase (different from zero almost everywhere in the considered objects) rather than on its Laplacian (which has large values only at the very edges) (see Eqs. (1) and (2)).

#172142 - $15.00 USD Received 10 Jul 2012; revised 2 Sep 2012; accepted 8 Sep 2012; published 29 Nov 2012

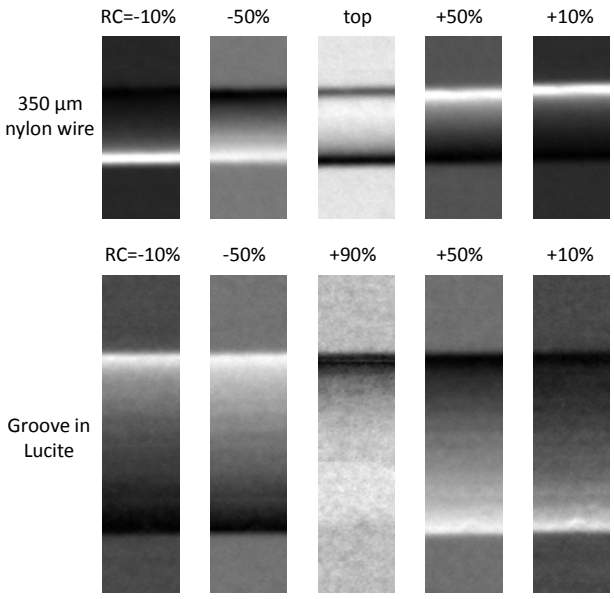

Fig. 5. AB images acquired at 5 different orientations of the analyzer crystal: expanded views in small regions of interest in the 350 µm diameter nylon wire and in the groove in the Lucite phantom.

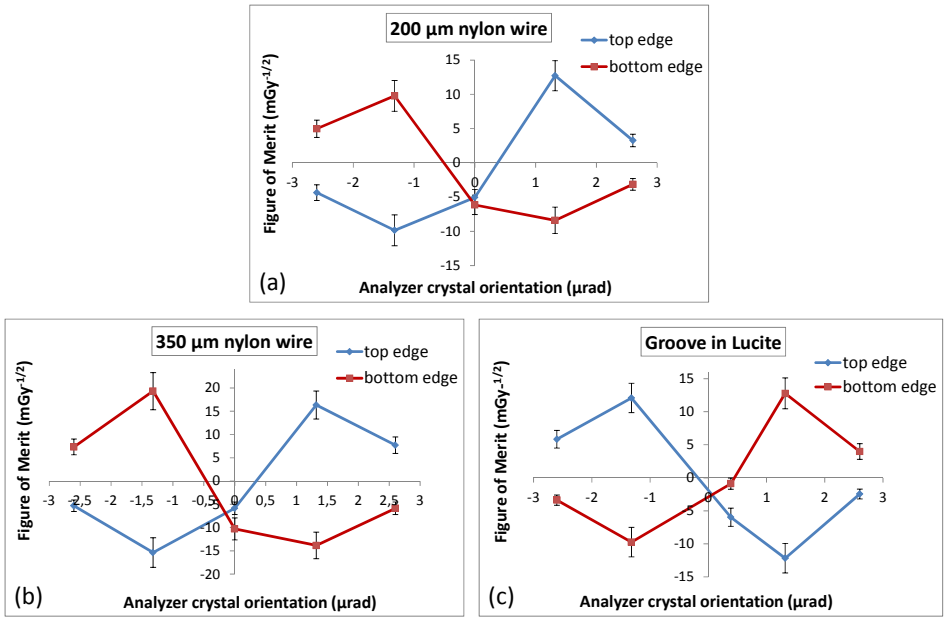

Fig. 6. Calculated values of the figure of merit (FoM) of the ABI edge signal for three different objects: (a) the 200 µm diameter nylon wire, (b) the 350 µm diameter nylon wire, (c) the groove in Lucite. Values at both the top and bottom edges are reported. The zero on the *x* axis corresponds to the Bragg condition (top) for the analyzer crystal.

For all phantoms the calculation of the FoM was carried out like in the case of PBI, independently for both the bottom and top objects edges (Figs. 6(a,b,c)). In all the three cases the highest FoM is achieved at the two positive and negative RC slopes, in agreement with what foreseen by the theory (Eq. (10) and Fig. 1(c)). The values are instead minimized at the top position and at the tails of the RC, where the RC first derivative is small. These results are

#172142 - $15.00 USD Received 10 Jul 2012; revised 2 Sep 2012; accepted 8 Sep 2012; published 29 Nov 2012

in agreement with previous experimental studies [24]. The reversed sign of the FoM values for the wires and the groove are due to the opposite directions of the refraction angles at their edges. Note that the positive values of the shown FoM are always slightly larger in modulus than the negative ones, differently from what predicted theoretically. One possible explanation is that the linear approximation of the RC is not very accurate when the refraction angles are large (like at the edges of the objects). In that case, the variations in the intensity for positive or negative displacements on the RC are not the same: they are in fact bigger when moving to angles corresponding to larger RC derivatives.

In ABI, the FoM presents the largest values in the case of the 350 μm nylon wire and its smallest values for the 200 μm wire and for the groove, while in PBI the largest values are provided by the 200 μm wire. This is again due to the different dependence of the two techniques on the phase shift (see Eqs. (1) and (9)). As a result, PBI ($FoM_{PBI} \propto \nabla^2\phi$) is more sensitive to high object frequencies, while ABI ($FoM_{ABI} \propto \partial\phi/\partial y$) is more sensitive to lower ones, as it was also experimentally shown by Pagot and associates [25]. Moreover, we also wish to remark that the FoM for ABI is considerably larger than that obtained in PBI (this fact is already evident from the images).

GI images of the horizontal 350 μm nylon wire and of the groove are reported in Fig. 7, for nine relative positions of the two gratings along one fringe period (note that the first and the last images have been acquired at exactly one period displacement, p_2 = 2.00 μm). Also in this case, the grayscale level has been adjusted independently for each image in order to optimize the object visualization.

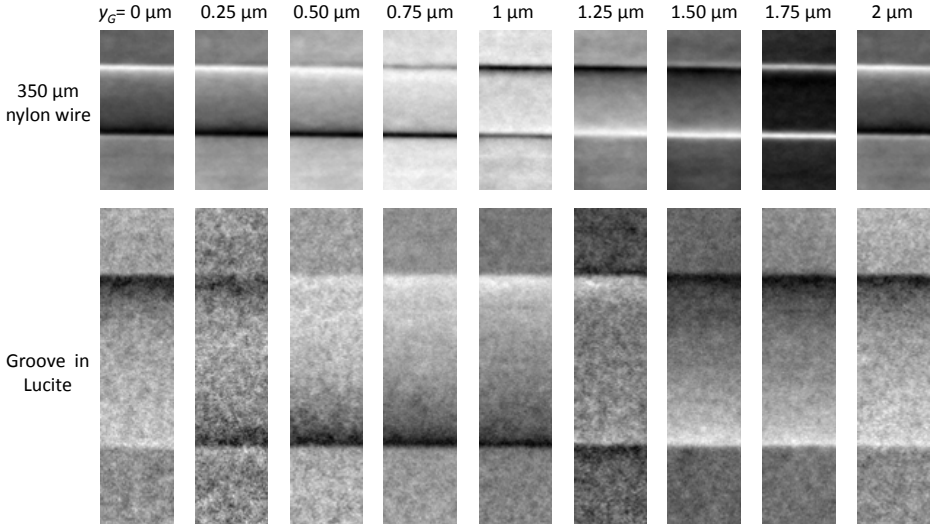

Fig. 7. GI images acquired at 9 different relative positions of the two gratings along one fringe period: expanded view in small regions of interest in the 350 μm diameter nylon wire and in the groove in the Lucite phantom.

The image contrast varies considerably depending on the corresponding position on the intensity curve *G* and in particular on the first and second derivatives of *G*. Images similar to those obtained at the RC slopes with the ABI technique can be observed at positions corresponding to the slopes of the intensity function *G* (y_G = 0.25 μm and y_G = 1.25 μm for the nylon wire and y_G = 0.75 μm and y_G = 1.75 μm for the groove) (Fig. 2(a)). Like for ABI, also in this case the contrast is reversed when moving from one slope to the other one since the first derivative of *G* has opposite signs at these points. Images acquired at the "top position" of the function *G* (at y_G = 0.75 μm and y_G = 1.00 μm for the nylon wire and at y_G = 0.25 μm for the groove) show a contrast similar to that obtained at the "top position" of the

#172142 - $15.00 USD Received 10 Jul 2012; revised 2 Sep 2012; accepted 8 Sep 2012; published 29 Nov 2012

RC since in this case the refracted X-rays are preferentially attenuated with respect to those that were not deviated. Interestingly, images showing an opposite type of contrast are obtained in GI at the "bottom position" of the intensity function G (for instance, image at y_G = 1.75 µm for the nylon wire). In this case, in fact, the X-rays refracted in both directions give rise to positive intensity variations in the image compared to the undeviated X-rays, as foreseen from the intensity curve in Fig. 2(a). This type of contrast is to some extent similar to the so-called dark-field imaging obtained in the variant of ABI employing Laue diffraction [26,27]. The "bottom position" image is also visible in the case of the groove (y_G = 1.25 µm) but the white GI refraction signal is here superposed to the black "propagation" contrast due to the finite sample-to-detector distance. Note that the various positions on the fringe period are shifted for the groove with respect to the wire because of a long term drift of the gratings over time (the two series of images were acquired a few hours apart).

The calculation of the FoM for the GI images was performed as for the PBI and ABI techniques. Results are presented in Fig. 8. The experimental FoM profiles resemble those obtained theoretically by using a linear approximation for the intensity function G (see Eq. (11) and Fig. 2(c)). Unlike the theoretical case, however, the experimental FoM values never go to zero because at both the "top" and "bottom" positions, where the first derivative of the function G vanishes, the linear approximation is inaccurate. In this case the equation for the FoM derived from a second-order Taylor expansion of the function G (Eq. (17)) can provide a better estimate.

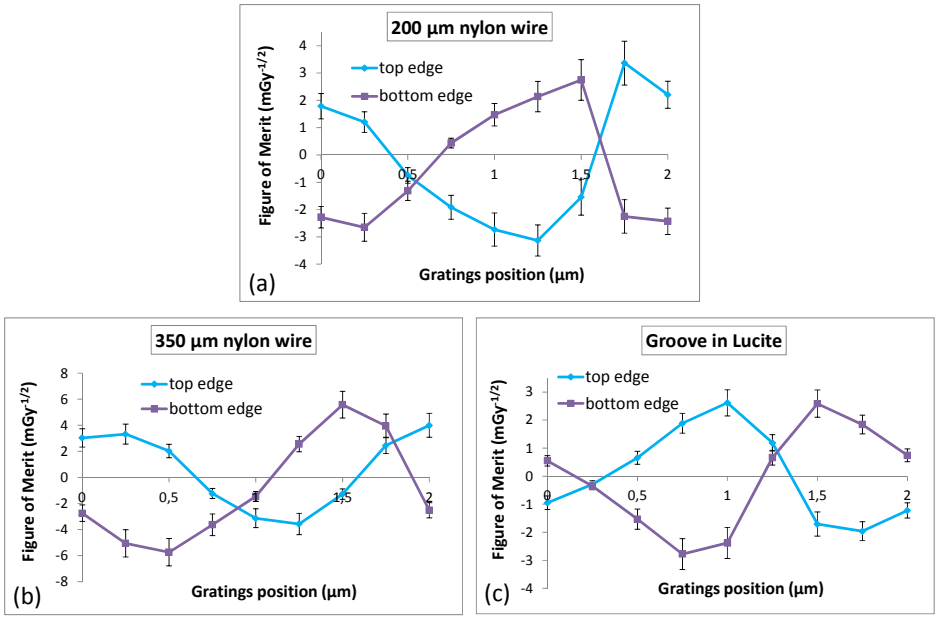

Fig. 8. Calculated values of the figure of merit (FoM) of the GI edge signal for three different objects: (a) the 200 µm diameter nylon wire, (b) the 350 µm diameter nylon wire, (c) the groove in the Lucite phantom. Values at both the top and bottom edges are reported.

Like in the ABI case, the largest FoM values are obtained for the thickest wire, while the thinner wire and the groove provide the smallest. This is not surprising since the two techniques are expected to be sensitive to the same physical quantity (the one-directional first derivative of the phase shift, to first approximation). Therefore the objects that give the largest signals for ABI are expected to provide the largest signals also for GI. By comparing the amplitude of the FoM values in the different techniques, we see that the values computed in GI are larger than those obtained from PB images but 3 to 5 times smaller than those obtained in ABI. By using Eq. (27), we had previously calculated (see section 4.1) the maximum

#172142 - $15.00 USD Received 10 Jul 2012; revised 2 Sep 2012; accepted 8 Sep 2012; published 29 Nov 2012

achievable FoM to be theoretically 8.7 times larger in ABI than in GI in our setup. The experimental values present, instead, smaller differences. This can be attributed to two causes: 1) the refraction angles at the edges of the considered objects are not small, thus the linear approximations of the RC and of the function *G* used to derive Eq. (27) are not fully accurate in this case; 2) the images, especially the ABI ones, have not been acquired at exactly the points of highest theoretical sensitivity (the curve of the theoretical ABI sensitivity is rather steep close to the maximum position, see Fig. 1(c)).

It is important to remark that the obtained results are dependent on the beam spatial coherence and on the spatial resolution of the used detector, in particular in the case of PBI. The measured intensity can be in fact expressed as a convolution between the ideal intensity and the imaging system PSF, as seen in section 2.2. This effect becomes important in phase-contrast images if the width of the PSF is comparable or larger than the typical size of the object edges. The smoothing due to the PSF is expected to affect the PBI signal to a higher degree with respect to the ABI and GI ones for two main reasons: a) the PBI edge signal, due its dependence upon the phase Laplacian, is narrower and b) the contiguous positive and negative peaks present in PBI tend to cancel each other (while this effect is not encountered in ABI and GI, where only one peak is present at the edge). This means for example that, if a smaller pixel size had been used, the SNR values in the case of PBI could have been much higher, while this would have presumably affected ABI and GI to a much lesser degree.

Finally, refraction angle images of the samples have been calculated from the ABI and GI images by using respectively the "Gaussian curve fitting" algorithm [28] and the phase-stepping method [8]. All the five images acquired at different positions of the RC have been used for ABI, and eight of the images acquired at different grating positions for GI. The results are presented in Fig. 9 for the 350 μm nylon wire and the groove in Lucite. The vertical profiles across the wire and the groove slightly differ for ABI and GI. In particular, the lowering and broadening of the edge peaks in the ABI profiles suggest in this case a degradation of the spatial resolution. This is compatible with the effect of the analyzer crystal PSF. The width of the analyzer PSF projected onto the detector, in fact, is equal to $2p\cdot\cos(\theta_{an})$, where p is the extinction depth of the crystal [29]. At a photon energy of 26 keV and for the Si(333) reflection, $2p\cdot\cos(\theta_{an})$ is equal to about 8.1 μm [17].

No artefacts related to setup instabilities could be detected in the obtained refraction images and in the extracted profiles, because of the very short duration of the image acquisition. However, these effects may be an issue and should be carefully considered when long acquisitions (e.g. tomography) are carried out. In this case the periodic recording of "whitefield" images (ABI and GI) and the retuning of the analyzer (ABI) may be necessary.

Peak edge FoMs have been calculated from these images, using the same method employed for the single PBI, ABI and GI images. The total radiation dose delivered to acquire the set of images used for extracting the refraction map has been considered. The calculated values are listed in Table 2. The largest FoMs are obtained for the 350 μm nylon wire and the lowest for the groove in Lucite. The calculated values are 2.7 to 3.7 times larger in ABI with respect to GI. These results are in agreement with those obtained for the single unprocessed images (see Figs. 4, 6 and 8).

#172142 - $15.00 USD Received 10 Jul 2012; revised 2 Sep 2012; accepted 8 Sep 2012; published 29 Nov 2012

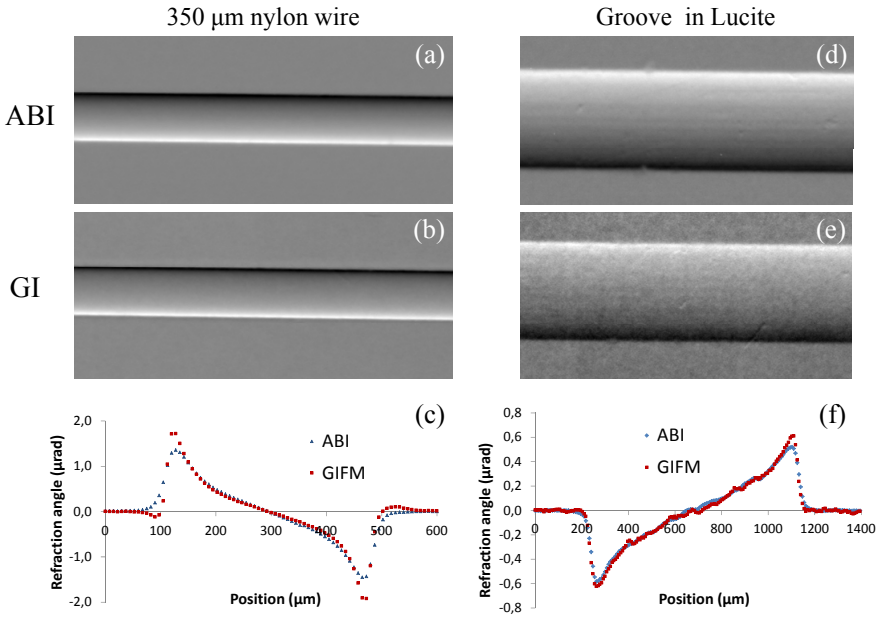

Fig. 9. Refraction angle maps calculated from AB images (with "Gaussian Curve Fitting" algorithm) and from GI images (phase-stepping method). a) 350 µm diameter nylon wire in ABI and b) in GI, c) vertical profiles across the wire, d) groove in Lucite in ABI and e) in GI, f) vertical profiles across the groove.

Table 2. Peak edge FoMs calculated for the refraction signal

	Refraction angle peak edge FoM ($mGy^{-1/2}$)	
	ABI	GI
350 µm wire	41 ± 8	15 ± 3
200 µm wire	28 ± 6	8 ± 2
Groove	19 ± 3	5 ± 1

5. Conclusions

We have presented a quantitative theoretical and experimental comparison of the signal-to-noise ratio (SNR) and figure of merit (FoM) for the edge signal in the PBI, ABI and GI phase-contrast techniques.

The two definitions for the SNR introduced in our previous work [11], the peak and the integral edge SNRs, have been recalled. Theoretical expressions for the corresponding peak and integral edge FoMs as a function of the experimental parameters and object properties have been derived.

The near-field regime approximation has been used in the derivation of expressions for PBI, while the linear approximation of the RC and of the function *G* have been considered respectively in ABI and GI. The latter approximation is only valid for small refraction angles and the condition for its validity is best satisfied at the slopes of the RC and *G* functions: at these points, in fact, their first derivative is maximized and the second derivative is equal to zero. At the "top" and "bottom" positions, however, the first derivative of these functions is equal to zero and the second derivative maximized, which results in inaccuracies in the linear approximation. For this reason, simple expressions for the FoM based on a second-order Taylor approximation have been proposed, which are expected to provide better results at these positions.

The expression for the peak edge FoM in PBI is dependent on the Laplacian of the phase shift induced by the object, while the ABI and GI FoMs are sensitive to the refraction angle

#172142 - $15.00 USD Received 10 Jul 2012; revised 2 Sep 2012; accepted 8 Sep 2012; published 29 Nov 2012

(which is proportional to the 1-D first derivative of the phase shift in the sensitivity direction). For this reason, PBI is expected to be more sensitive to higher object frequencies than ABI and GI. The integral edge FoM, instead, is proportional in all cases to the same object quantity, the phase shift, and thus provides a way to directly compare the signal obtainable in the three techniques. By using the theoretical expressions for the integral edge FoM, the sensitivities of the three techniques, in terms of the smallest phase shift that they can detect, have been compared and their dependence upon the different acquisition parameters analyzed.

The expected FoM values achievable under the experimental and acquisition conditions used for our experiment have been theoretically calculated. It results that ABI provides a better sensitivity with respect to the PBI and GI techniques. We have discussed how the FoM can vary by changing the acquisition parameters in each of the techniques. The considered parameters include the propagation distance in PBI, the crystal reflection in ABI and the distance between the gratings in GI. The dependence upon the projected source size, the system-object smoothing parameter σ and the X-ray energy have been also investigated. In particular, PBI can provide large FoM values when high spatial resolutions are considered (small projected source size, high-resolution detector and objects with sharp edges), but for low spatial resolution the interference fringes are rapidly smeared out and the sensitivity of the method decreased. The dependence of GI upon the smoothing parameter σ is weaker than in PBI; however, it is strongly affected by the projected source size. ABI sensitivity, instead, is affected to a lower extent by the two parameters. Also the dependence on the energy is different for the three phase-contrast techniques. In particular, the decrease of the signal with the X-ray energy is slower for ABI than for the other two techniques. At high X-ray energies, therefore, ABI is expected to provide much larger sensitivity than PBI and GI.

An experimental verification has been carried out on test objects of known materials and geometry. Results are in agreement with the theoretical predictions. The PBI FoM increases linearly with the propagation distance in the near-field diffraction regime, while ABI and GI FoMs appear to be strongly dependent upon the chosen working position along the RC and the function G, respectively. The largest values are obtained around the slopes of these functions, where the first derivative reaches the largest values. As theoretically predicted, the ABI technique provided the largest and the PBI technique the smallest FoM values in our experimental setup.

Finally, it is remarkable that the largest FoMs are not achieved for the same test object by the three techniques. In PBI the largest signal is obtained with the smallest wire, while in ABI and GI the largest signal is obtained with the biggest wire. This can be attributed to the fact that, due to its different dependence upon the object phase shift, PBI is sensitive to higher object frequencies than both ABI and GI do.

Future work will focus on extending this comparison to different kinds of biological samples, with the aim of analyzing and investigating the potential of these different phase-contrast techniques for various biomedical applications.

Acknowledgments

We acknowledge the European Synchrotron Radiation Facility (ESRF) for provision of beamtime and the support through the DFG - Cluster of Excellence Munich-Centre for Advanced Photonics. Authors also thank Dr. E. Ziegler, Dr. H. Requardt and T. Brochard for their help in the preparation of the experimental set-ups, and Dr. C. David for supplying the gratings used in the experiment. Dr. F. Pfeiffer, Dr. T. Weitkamp and Dr. M. Bech are acknowledged for their assistance in the GI acquisitions and useful discussions.

#172142 - $15.00 USD Received 10 Jul 2012; revised 2 Sep 2012; accepted 8 Sep 2012; published 29 Nov 2012